Experimental and analytical studies on shear behaviors of FRP-concrete composite sections

Zou, Xingxing; Feng, Peng ; Bao, Yi; Wang, Jingquan ; Xin, Haohui

DOI
10.1016/j.engstruct.2020.110649

Publication date
2020

Document Version
Accepted author manuscript

Published in
Engineering Structures

Citation (APA)
Zou, X., Feng, P., Bao, Y., Wang, J., & Xin, H. (2020). Experimental and analytical studies on shear behaviors of FRP-concrete composite sections. *Engineering Structures*, *215*, Article 110649. https://doi.org/10.1016/j.engstruct.2020.110649

Experimental and analytical studies on shear behaviors of FRP-concrete composite sections

Xingxing Zou[1], Peng Feng[2], Yi Bao[3], Jingquan Wang[4*] and Haohui Xin[5]

[1] Department of Civil, Architectural & Environmental Engineering, Missouri Univ. of Science and Technology, Rolla, MO 65409. E-mail: zxbn4@mst.edu

[2] Department of Civil Engineering, Tsinghua University, Beijing 100084, China; E-mail: fengpeng@tsinghua.edu.cn

[3] Department of Civil, Environmental and Ocean Engineering, Stevens Institute of Technology, Hoboken, NJ 07030. E-mail: yi.bao@stevens.edu

[4] Key Laboratory of Concrete and Prestressed Concrete Structures of the Ministry of Education, Southeast University, Nanjing 210096, China. E-mail: wangjingquan@seu.edu.cn (corresponding author)

[5] Faculty of Civil Engineering and Geosciences, Delft University of Technology, Delft, the Netherlands, E-mail: h.xin@tudelft.nl

ABSTRACT

The design of FRP profile-concrete composite sections, including beams and decks, is usualy governed by the shear strength of the FRP profiles. However, analytical methods that can precisely predict the shear capacity of the composite sections have not been well developed, because there is lack of knowledge of the FRP-concrete composite action and distribution of shear stress along the FRP. This paper investigates the shear behaviors of FRP-concrete composite sections and develops formulae to predict the shear capacity of the composite sections. First, flexural tests of three FRP-concrete composite beams were conducted to investigate the shear failure mode and interface behaviors. All the beams failed in FRP shear fracture along horizontal direction. Then, push-out tests were used to determine the slip property for the FRP-concrete interface which reveals that FRP stay-in-place form and steel bolts can ensure full and partial composite action, respectively. Based on the experimental study, closed-form equations to compute the maximum shear stress are derived and validated against experimental data in this paper and literature. Finally, simple yet reliable equations of shear capacity are derived and recommended for engineers to design the FRP-concrete composite sections.

Key words: shear capacity; FRP-concrete composite sections; composite action; slip effect; shear connection.

Notation

A_{web} = cross sectional area of FRP web(s);
A_C, A_F = cross sectional area of concrete and FRP, respectively;
$A_F(y)$ = parameter in equations;
b = shear span length of beam specimens;
b_C, b_F = width of concrete slab and FRP flange, respectively;
E_C, E_{Fx} = elastic modulus of concrete and FRP (in longitudinal direction), respectively;
h_0 = distance between the neutral axis of concrete and FRP;
h_C, h_F = height of concrete and FRP, respectively;
I_C, I_F = moment inertia of concrete and FRP, respectively;
k = smeared slip modulus of the interface;
K = slip modulus per connector;
L = beam span;
$m(x)$ = ratio given by $m(x) = h_0 ks(x)/V(x)$;
m_0 = value of $m(x)$ at the support points of beams;
m_{full} = value of m_0 with full composite action;
$M_C(x)$, $M_F(x)$ = flexural moment carried by concrete and FRP, respectively;
n = number of rows of the connector in lateral direction;
n_0 = number of studs in one push-out test specimens;
$N_C(x)$, $N_F(x)$ = axial force in concrete and FRP, respectively;
p = longitudinal space between two adjacent connectors;
P = total applied load;
P_u = experimental ultimate load;
$r(x)$ = distributed normal force along FRP and concrete interface;
$s(x)$ = interfacial slip;
s_0 = slip at the load of $0.5P_u$ of push-out test;
s_{max} = maximum slip;
S_{xy} = shear strength of FRP web(s);
$S_F(y)$, $S_F(y)$ = parameters in equations;
$t(y)$ = thickness of FRP web or FRP width;

t_{web} = thickness of FRP web;
V_1, V_2 = shear capacity computed by Eq. (1) and Eq. (2), respectively;
$V(x), V_C(x), V_F(x)$ = shear force carried by the composite section, concrete and FRP, respectively;
V_{test} = experimental shear capacity of beam specimens;
X_c = compressive strength of FRP;
y_0 = vertical coordinate of the location of maximum shear stress;
$y_{0,ana}$ = analytical value of y_0;
$y_{0,test}$ = experimental value of y_0;
$\alpha, \beta, A_0, A_1, I_0$ = parameters used to simplify the equations;
α_E = ratio of E_{Fx} over E_C;
α_1 = ratio of cross sectional area of FRP flanges over concrete;
α_2 = ratio of h_F and h_C;
δ_u = maximum mid-span deflection;
$\varepsilon_C(x,y), \varepsilon_F(x,y)$ = strains of concrete and FRP, respectively;
$\varepsilon_{slip}(x)$ = strain difference caused by the slip at FRP-concrete interface;
η_C, η_F = contribution ratio of concrete and FRP, respectively;
η_{SD} = ratio of maximum shear stress over average shear stress;
$v(x)$ = distributed interfacial shear force along longitudinal direction;
$\sigma_F(x,y)$ = normal stress of FRP;
$\tau_C(x,y), \tau_F(x,y)$ = shear stress of concrete and FRP, respectively;
τ_{max} = maximum shear stress;
ϕ = curvature of the beam.

1. Introduction

Fiber reinforced polymer (FRP) has extraordinary mechanical and in-service properties, which can improve the stiffness, strength, durability, life-cycle cost, and environmental impacts when combined with other construction materials [1]. Recently, there are increasing research interests and filed applications of FRP profiles-concrete composite (or hybrid) structures, particularly in the forms of bridge decks [2], girders [3][4], and floor systems [5][6]. The FRP-concrete systems maximize the advantages of the materials by integrating FRP that is extremely durable and lightweight with concrete that is low-cost and has desired compressive strength [7][8]. Among various FRP-concrete systems, FRP-concrete composite beams/decks (see Fig. 1) demonstrated superior cost-effectiveness and high durability, compared with traditional steel-concrete composite structures and all-FRP structures [1][3][4][9][10][11]. Hereafter, FRP-concrete composite (or hybrid) beam/deck is referred as FRP-concrete composite section for a general meaning. The concrete slab is cast on top of an FRP profile (see Fig. 1). The concrete and FRP are joined by interfacial shear connection such as epoxy adhesives [5], perforated FRP ribs [2][9], steel bolts [3][11], FRP bolts [3], or FRP shear keys [4][8]. Flexural tests showed that glass FRP (GFRP)-concrete composite beams had higher stiffness and strength, compared with all GFRP profiles [12]. On the other side, compared to the equivalent reinforced concrete (RC) beams, the hybrid GFRP-concrete specimens displayed approximate 50% higher ultimate capacity with 50% less weight [12].

Pultrusion is a cost-effective and efficient technique to manufacture FRP profiles with high quality control [1]. Pultruded FRP profiles have been widely used in FRP-concrete composite sections [13][14][15]. Although FRP-concrete composite sections follow the same concept as steel-concrete composite sections, a salient difference is that the shear strength of pultruded FRP is fairly lower than that of steel profiles (see Table 1) [16][17][18][19]. Owing to the low shear strength, flexural tests on FRP-concrete composite sections often induce undesirable and catastrophic shear failure at FRP web or web-top flange junction at relatively low load levels [8][12][20][21]. Both GFRP-concrete interface failure and shear failure in GFRP webs have been observed from existing tests [20]. The GFRP-concrete bond failure can be avoided by developing effective shear connectors [8][9][22][23][24]. Therefore, the shear capacity usually governs the design of the FRP-concrete composite sections, which means precisely computing the shear capacity plays a critical role in the design.

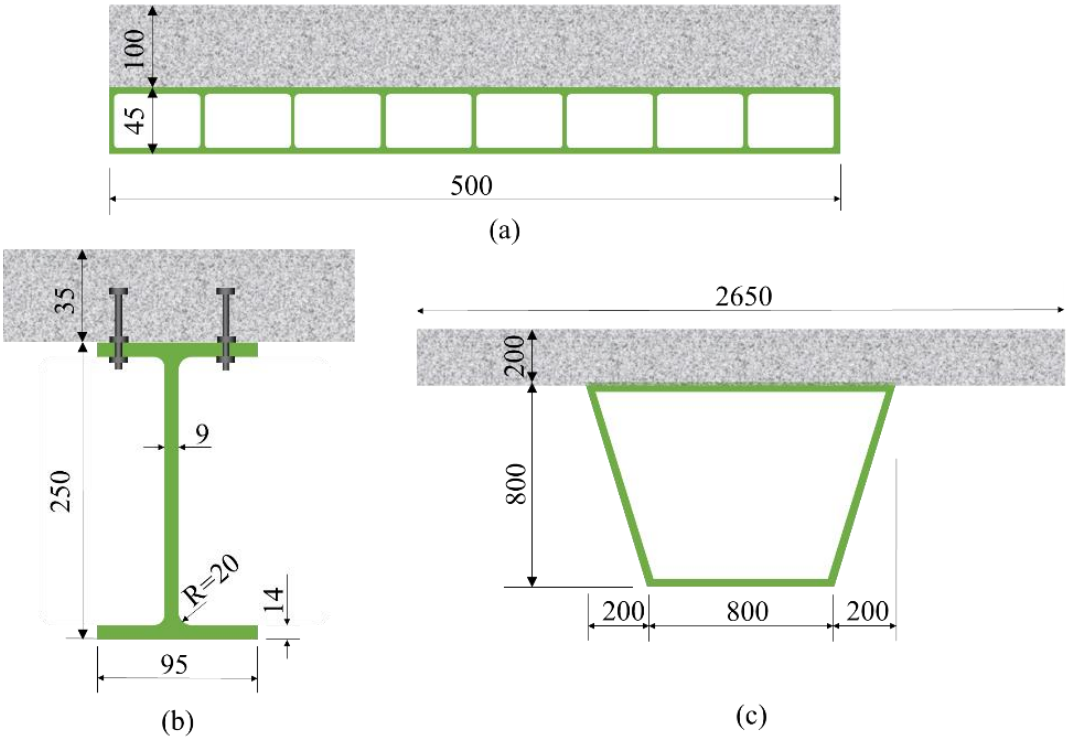

Fig. 1. Typical cross section of: (a) FRP-concrete hybrid deck [2]; (b) open-section FRP-concrete hybrid beam [3]; and (c) closed-section FRP-concrete hybrid beam [4]. Unit in mm.

Table 1. Typical ratio of shear strength (S_{xy}) and compression strength (X_c) of FRP and steel

Profile	Company	S_{xy} (MPa)	X_c (MPa)	S_{xy}/X_c
GFRP	Fiberline [16]	31	240	1/8
GFRP	Strongwell [17]	31	207	1/7
GFRP	Topglass [18]	25	220-230	1/12～1/9
GFRP	Creative Pultrution [19]	23-31	227-316	1/14～1/7
Steel		135	235 (Yield)	1/1.7

Currently, all the existing methods for the shear capacity of FRP-concrete composite sections neglect the shear resistance of the concrete slab [20][21]. It is reasonable to neglect the shear resistance of the concrete slab in steel-concrete composite beams, because the shear strength of the steel beam is typically much higher than that of the concrete. However, since the shear strength of FRP profile is typically low, neglecting the shear resistance of concrete may significantly compromise the accuracy of the analysis. For example, it was assumed in [21] that the shear force was carried only by the FRP webs, and the shear stress was uniform along the height of the FRP webs. Accordingly, the shear capacity of FRP-concrete composite sections was expressed as:

$$V_1 = A_{web} S_{xy} \tag{1}$$

where V_1 is the shear capacity; A_{web} is the total cross sectional area of the FRP web(s); S_{xy} is the shear strength of the FRP web(s). However, the assumption of the uniform shear stress distribution is not consistent with the reality. Hence, it was assumed in [20] that the maximum shear stress in FRP webs was 1.5 times the average shear stress. So, the shear capacity was expressed as:

$$V_2 = \frac{2}{3} A_{web} S_{xy} \tag{2}$$

where V_2 is the shear capacity. Table 2 shows the test results of 12 specimens with a shear failure at FRP web(s) or top-flange-web joints [5][8][12][21]. Eqs. (1) and (2) underestimated the shear capacity by 18% and 45%, respectively. There is a need to develop a more accurate method to predict the shear capacity of the FRP-concrete composite sections.

Table 2. Comparison between analytical [Eqs. (1) and (2)] and experimental results of shear capacity

Reference	Specimen	Profile depth (mm)	Web thickness (mm)	Web area (mm^2)	S_{xy} (MPa)	V_1 (kN)	V_2 (kN)	V_{test} *a (kN)	$\frac{V_1}{V_{test}}$	$\frac{V_2}{V_{test}}$
[8]	HB	150	10	1500	25.3	37.5	25.0	49.6	0.76	0.50
	HB-T	150	10	1500	25.3	37.5	25.0	74.8	0.50	0.33
	HB-R	150	10	1500	25.3	37.5	25.0	47.3	0.79	0.53
[21]	Beam C*-S	228.6	11.1×2	5075	31.0	157.3	104.9	170.5	0.92	0.62
	Beam S*-S	228.6	11.1×2	5075	31.0	157.3	104.9	191.5	0.82	0.55
[5]	HB1	200	10	2000	47.1*b	94.2	62.8	91.00	1.04	0.69
	HB3	200	10	2000	47.1*b	94.2	62.8	148.10	0.64	0.42
	HB5	200	10	2000	47.1*b	94.2	62.8	87.90	1.07	0.71
[12]	M2-HB1	120	8	960	35.0	33.6	22.4	39.00	0.86	0.57
	M2-HB2	120	8	960	35.0	33.6	22.4	37.67	0.89	0.59
	M2-HB3	120	8	960	35.0	33.6	22.4	44.88	0.75	0.50
	M2-HB4	120	8	960	35.0	33.6	22.4	45.63	0.74	0.49
Average									0.82	0.55

*a. V_{test} is the test result of the shear capacity of the specimens.
*b. The value was provided by the authors of [12].

This paper investigates the shear behavior of FRP-concrete composite sections and develops formulae to accurately predict the shear capacity of the composite sections, aiming to advance the fundamental understandings of the composite behaviors and provide effective tools for the design and evaluation of FRP-concrete composite sections.

2. Method

This study aims at more advanced understanding of the shear behavior of FRP-concrete hybrid sections and proposing a design method for the shear capacity considering the contribution of concrete. Experimental tests were conducted in four-point bending, where the specimens were designed to be failed in shear. An analytical approach, returned to the fundamental analysis of composite action, was proposed to compute the shear stress of the specimen. The results of maximum shear stress given by derived equations were compared against the experimental results. Based on the experimental study and the analytical approach, closed-form equations of the shear capacity of the composite sections were derived, considering the contribution of concrete and interfacial slip. Finally, methods and equations that can be conveniently applied to design the FRP-concrete composite sections were explored.

3. Experimental Investigation

This section presents the flexural test of FRP-concrete composite beams and push-out test of FRP-concrete connectors. Subsection 2.1 introduces the materials and properties. Subsection 2.2 introduces the flexural test. Subsection 2.3 introduces the push-out test.

3.1. Materials

FRP profiles (see Fig. 2a) were made from unsaturated polyester resin reinforced by glass fibers through pultrusion technique. The FRP products are commercially available at the Nanjing Kangte Composite Material Co., Ltd., in Nanjing, China [25]. The fiber layout of the FRP profiles is unidirectional roving in the core sandwiched between two layers of continuous-strand mats along the outer surfaces (see Fig. 2a). The mass percentage of fibers is approximate 45%, the mass percentage of resin is 35%, and the left is $CaCO_3$ powder filler, according to the manufacturer.

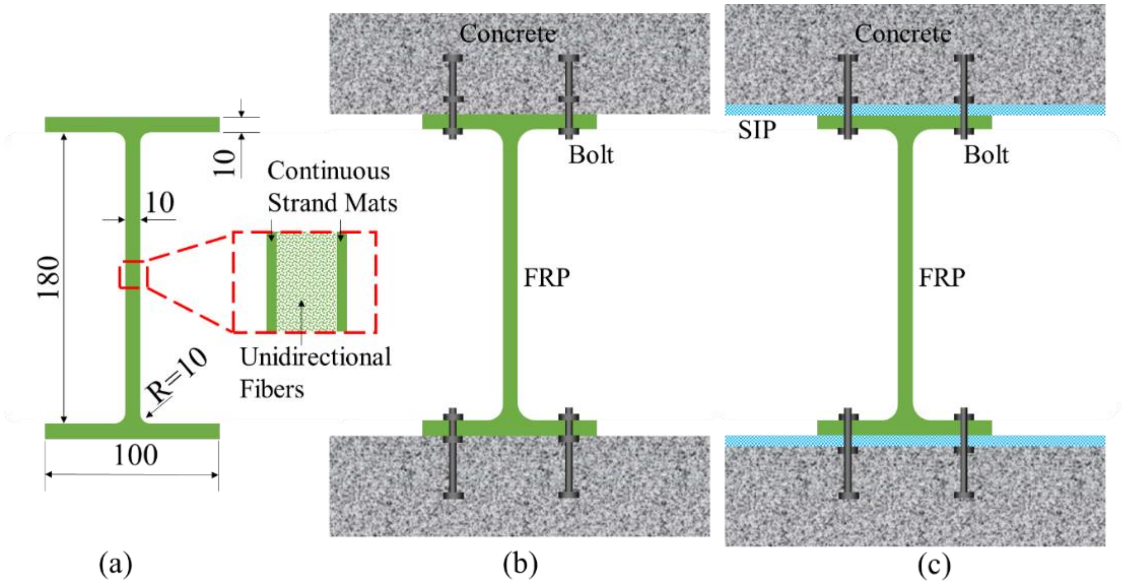

Fig. 2. Cross sections of: (a) FRP profile, (b) push-out test specimens of Group I &II, and (c) push-out test specimens of Group III. SIP stands for stay-in-place formwork.

The density of the profiles is 1,900 kg/m^3, as specified by the manufacturer. The tensile, compressive, and shear properties were obtained through testing tensile, compressive, and short three-point bending coupons, respectively, according to Chinese standard GB 50608–2010 [26]. The coupons were cut from the actual pultruded profiles and machined to the exact dimensions. The longitudinal tensile and compressive strengths were 420 MPa and 350 MPa, respectively. The longitudinal tensile and compressive moduli were 25 GPa and 23 GPa, respectively. The shear strength was 9.2 MPa, which is lower than other commercial products shown in Table 1. The low shear strength is attributed to the lack of multi-directional fibers on the webs and the use of $CaCO_3$ powder as the filler in the resin matrix.

The concrete was designed to achieve a compressive strength of 30 MPa at 28 days. The specimens were cast and tested in accordance with Chinese standard GB 50010–2010 [27]. The average values of the elastic modulus, compressive strength, and compressive strain at peak stress of the concrete were 28.2 GPa, 29.5 MPa, and 0.00263, respectively. All push-out and flexural specimens were cured under identical condition as the coupons for material properties testing.

Steel bolts (see Figs. 2b and 2c) were fixed on the top flanges of the FRP profiles using nuts and washers on both sides of the FRP flange plate. The steel bolts serve as headed studs that integrate the concrete and FRP. The grade of the steel was Grade M10 8.8 with the tensile and yield strengths of 800 MPa and 640 MPa, respectively. For the meaning of the Grade Ma $b.c$, the diameter of the stud shank is a mm, the tensile strength is $b\times100$ MPa, and the ratio of yield strength over tensile strength is $c\times0.1$. The steel stud in this study had a diameter of 100 mm. The embedded length in concrete, defined as the distance from the top of the stud to the top of the FRP flange, was 80 mm. Steel washers, with an outer diameter of 20 mm, inner diameter of 10.5 mm (slightly larger than the diameter of the studs) and a thickness of 2 mm, were used to distribute the local stress caused by axial pre-tightening force of the studs.

3.2. Flexural test of FRP-concrete composite beams

Three FRP-concrete composite beams were tested, as shown in Fig. 3. Each beam was composed of an I-shaped pultruded GFRP beam (see Fig. 2a, Fig. 3a) and a concrete slab (see Fig. 3). All specimens were simply supported and loaded under four-point bending. The deflections and the slippages were measured by linear variable differential transformers (LVDTs). The strains in FRP and concrete were measured by strain gauges. Two LVDTs were used to measure the horizontal displacements of FRP and concrete, respectively, and the different horizontal displacements indicated the interfacial slip. The web thickness (t_{web}) and flange thickness (t_{Flange}) of the FRP profile were 10 mm. The transversal space of the steel studs was 55 mm.

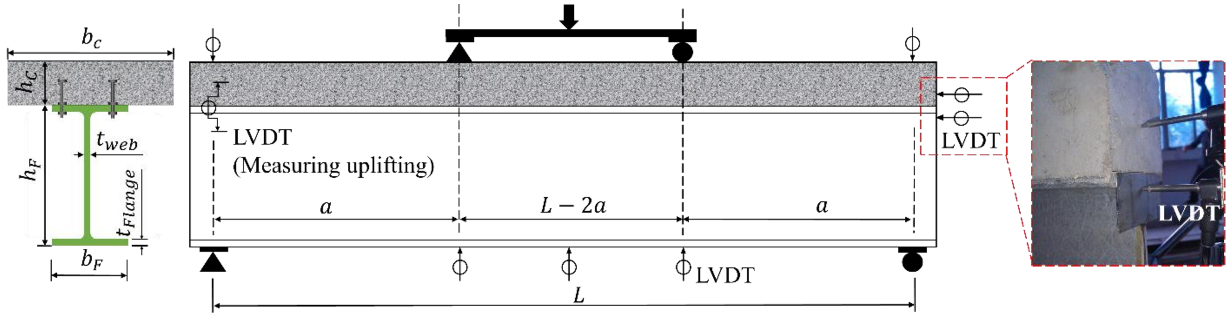

(a) (b) (c)

Fig. 3. FRP-concrete composite beam: (a) cross section, (b) side view, and (c) deployment of the LVDTs measuring slip.

The specimens were fabricated in four steps: (i) drill holes in the upper flanges of FRP profiles (see Fig. 4a), (ii) install steel studs at the predefined locations (see Fig. 4b), (iii) fabricate the wood formwork (see Fig. 4c), and (iv) cast concrete slab.

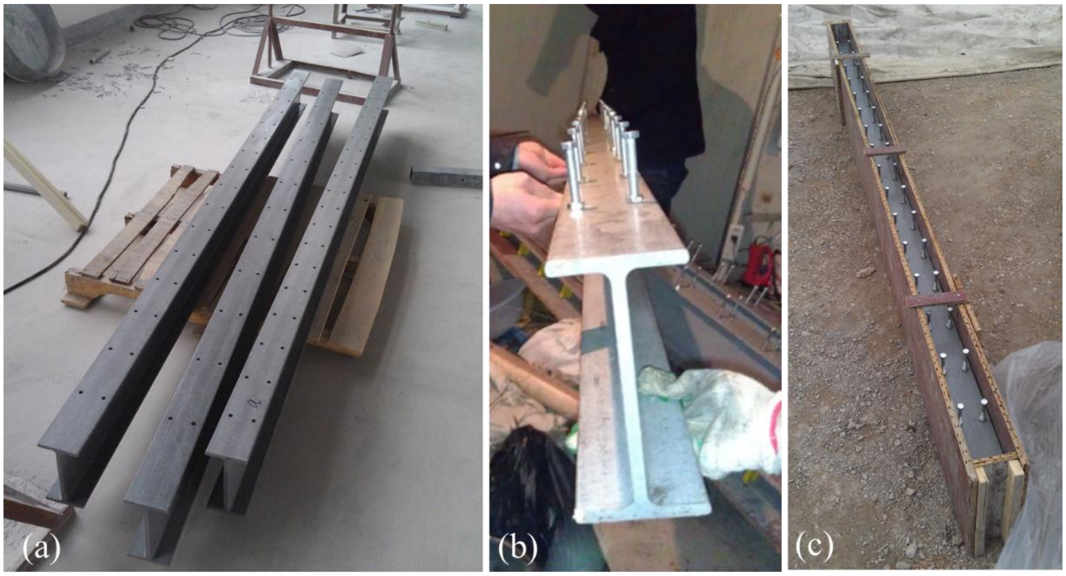

Fig. 4. Construction of FRP-concrete composite beam specimens: (a) FRP beams with drilled holes, (b) an FRP beam with steel studs, and (c) wood forms.

Similar failure processes and modes were observed from the three specimens. Before the failure, there was no notable acoustic activities and visible cracks. As the load reached the ultimate capacity, a crack on FRP web occurred from the support and suddenly propagated to the mid-span in a few seconds (see Fig. 5), resulting in a catastrophic and brittle failure.

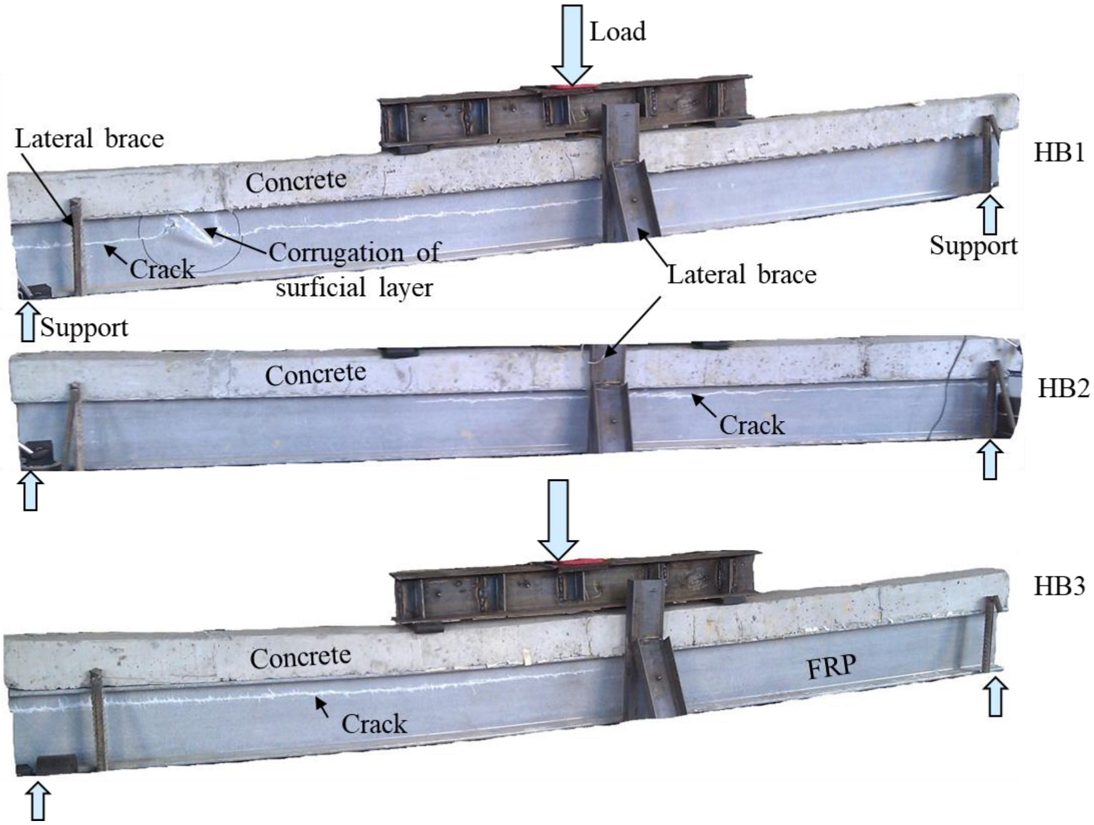

Fig. 5. Failure modes of the FRP-concrete composite beam specimens tested under four-point bending.

The results are summarized in Table 3, where P_u is the experimental ultimate load, $y_{0,test}$ is the average vertical coordinate (the coordinate system will be introduced in the next section) of the main crack (see white lines in Fig. 5), $y_{0,ana}$ is the value which will be introduced in next section, δ_u is the maximum mid-span deflection, and s_{max} is the maximum slip.

Table 3. Results of flexural tests

Specimen	h_C (mm)	b_C (mm)	P_u (kN)	$y_{0,test}$ (mm)	$y_{0,ana}$ (mm)	$\frac{y_{0,ana}}{y_{0,test}}$	δ_u (mm)	s_{max} (mm)
HB1	100	100	37.4	-56.5	-49.28	0.87	16.7	0.060
HB2	100	100	39.0	-61.5	-55.78	0.91	17.7	0.219
HB3	100	100	35.7	-58.6	-61.48	1.05	16.3	0.236

The load-deflection curves are plotted in Fig. 6a. The load increases approximately linearly with the mid-span deflection until the brittle shear failure. The load-slip relationships are plotted in Fig. 6b. The slip of HB1 was less than 0.06 mm, smaller than the rest two specimens, because HB1 had more steel studs as the shear connection. The slips of HB2 and HB3 were close, with a maximum value of 0.219 mm and 0.236

mm, respectively. The interfacial uplifting - vertical separation, measured by the vertical LVDT at the left side of the beam in Fig. 3b - was almost zero for all the beams during the loading.

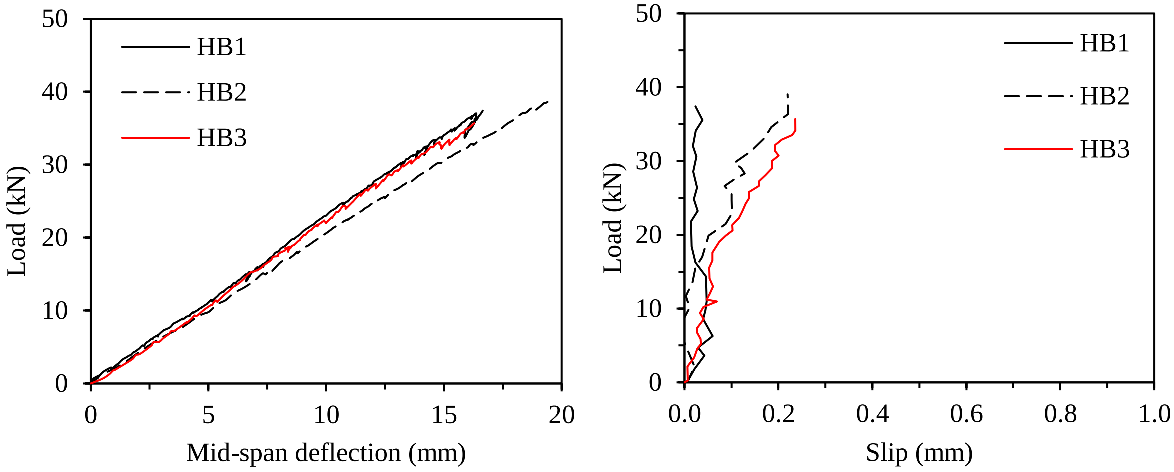

(a) (b)

Fig. 6. Test results of FRP-concrete composite beam specimens: (a) load-deflection responses, and (b) load-slip responses.

3.3. Determining slip modulus from the load-slip response of push-out specimens

In order to consider the slip between FRP and concrete, the slip stiffness for each connector, K, was experimentally determined through push-out tests (see Figs. 2b and 2c), as reported in [8]. Three groups of connectors were tested, namely Groups I, II, and III. Group I had ordinary steel studs (SB), Group II had high steel studs (HSB, the same as the studs used in beam test of this paper, see Section 2.2), and Group III used stay-in-place formwork (see Fig. 2c) between the FRP and concrete. The formwork provided bond with the concrete slab and eased the construction of concrete. Groups I and II showed two failure modes, namely the studs shank shear fracture and shear-out failure of FRP flange, as elaborated in [24]. Fig. 7 plots the load-slip response, which is a pivotal factor to evaluate the composite action of the FRP-concrete composite sections. The secant slope at half of the ultimate load, $0.5P_u$, is defined as slip modulus – K (see Fig. 7), which is given as:

$$K = \frac{0.5P_u}{n_0 s_0} \tag{3}$$

where n_0 is the number of studs in a push-out test; s_0 is the slip at the load $0.5P_u$. Table 4 lists the results of K of push-out specimens in [5][8][24].

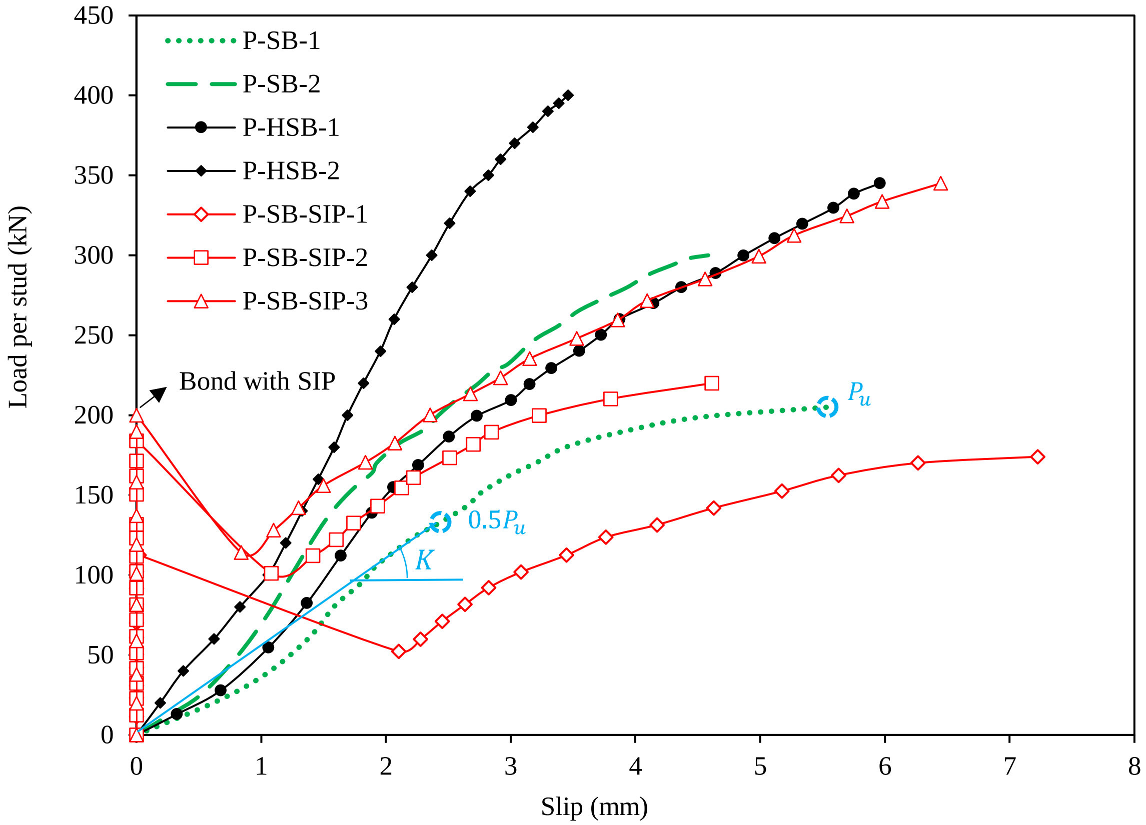

Fig. 7. The relationship between the load per stud and interfacial slip between FRP and concrete. The bond between the SIP and concrete caused a zero-slip phase at the beginning of loading.

Table 4. Parameters and results of push-out tests

Reference	Specimen	n_0	p (mm)	Studs	$0.5P_u$ (kN)	s_0 (mm)	K (kN/mm)
[8]	P-SB-1	8	200	M10 4.6	105	1.91	6.87
	P-SB-2	12	150	M10 4.6	150	1.73	7.23
	P-HSB-1	8	200	M10 8.8	170	2.26	9.40
	P-HSB-2	12	150	M10 8.8	200	1.69	9.86
[24]	Specimen 1	4	150	M10 6.8	47.9	2.13	5.70
	Specimen 2	4	150	M10 6.8	61.0	2.74	5.65
	Specimen 3	4	150	M10 6.8	61.4	2.31	6.67
	Specimen 4	4	150	M10 6.8	46.9	3.78	3.09
	Specimen 5	4	150	M10 6.8	55.3	2.54	5.53
[5]	SCS1	4	200	M8 8.8	40	0.92	10.87
	SCS2	4	200	M10 8.8	80	1.00	20.00
	SCS3	4	200	M10 8.8	60	1.25	12.00

4. Analytical Study on Shear Capacity

This section conducts analytical study on the shear behavior of FRP-concrete composite sections considering slip effect and the distribution of shear stress in the FRP profile. Subsection 3.1 investigates the interfacial slip behaviors. Subsection 3.2 investigates the shear stress distributions in FRP and concrete considering the interfacial slip. Subsection 3.3 shows the validation of analytical results against the tests.

4.1. Interfacial slip

Similar to steel-concrete composite sections [28], an FRP-concrete composite section is composed of an FRP profile and a concrete slab that are discontinuously connected, as shown in Fig. 8. Mechanical analysis is conducted to analyze the FRP-concrete composite section based on the following assumptions:

(i) Only the shear connectors and SIP formwork contribute to the shear connection between the FRP and concrete. The discrete connectors were smeared to the whole length of the interface, which is similar to the analysis of steel-concrete composite sections [29][30][31]. By so doing, the model does not distinguish between discontinuous and continuous layers connection. For the specimens with epoxy shear connection [32], FRP shear keys [8], and perforated FRP ribs [24], the interface has full composite action, because the slip is very small compared with the specimens with steel bolts.

(ii) The curvature and deflection of the FRP and concrete are the same. In other words, there is no vertical separation (uplifting effect) at the interface, which has been the test results in Section 2.2.

(iii) Bernoulli's hypothesis on strain distribution is applicable to sections of FRP and concrete separately, i.e., the shear deformation has been neglected, this may cause some error so the influence will be discussed according to experimental test.

According to assumption (i), Eqs. (4) and (5) are obtained:

$$v(x) = ks(x) \tag{4}$$

$$k = nK/p \tag{5}$$

where $v(x)$ is the distributed interfacial shear force (see Fig. 8); x is the longitudinal coordinate with the origin at support point; k is the smeared slip modulus of the interface; $s(x)$ is the interfacial slip (see Fig. 8); n is the number of rows of the connector in lateral direction; K is the slip modulus per connector defined by Eq. (3) from the push-out tests (see Fig. 7); p is the longitudinal space between two adjacent connectors.

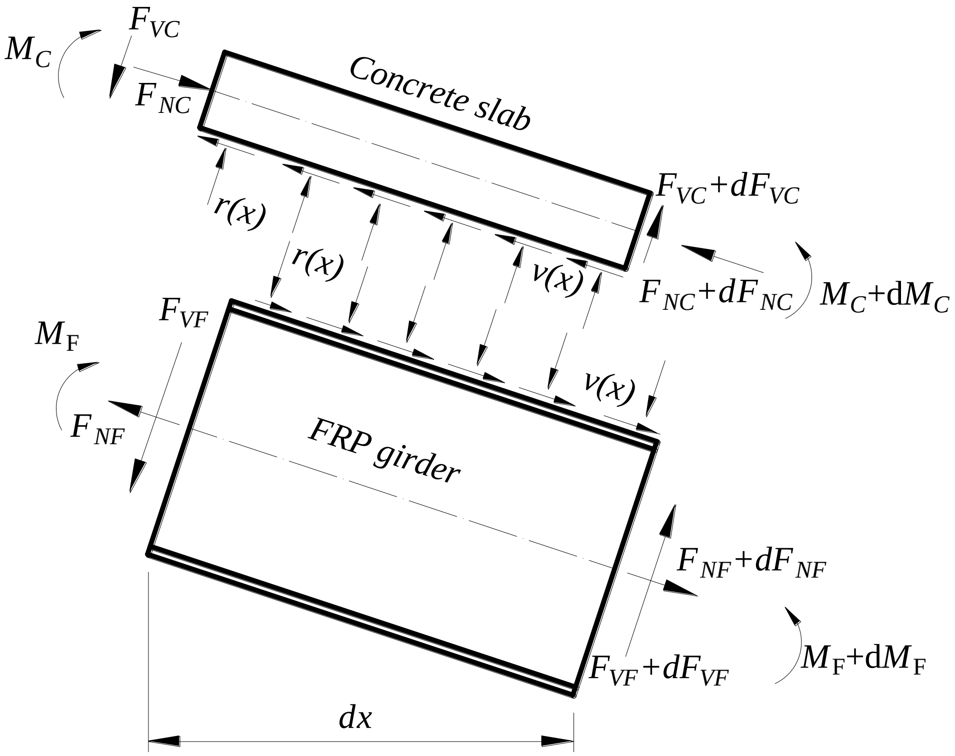

Fig. 8. Model of sectional analysis of section *dx*.

According to equation of equilibrium of the infinitesimal (*dx*), in the horizontal (*x*) direction:

$$\frac{dN_C(x)}{dx} = \frac{dN_F(x)}{dx} = -v(x) \tag{6}$$

where $N_C(x)$ and $N_F(x)$ are the axial forces carried by concrete and FRP, respectively.

According to equation of equilibrium of the infinitesimal (*dx*), in the vertical (*y*) direction, the shear force satisfies:

$$V_C(x) + V_F(x) = V(x) \tag{7}$$

where $V_C(x)$ and $V_F(x)$ are the shear forces carried by the concrete and FRP, respectively; $V(x)$ is the total shear force. Under three-point bending (Fig. 9a) or four-point bending (Fig. 9b): $V(x) = P/2$, where P is the total applied load.

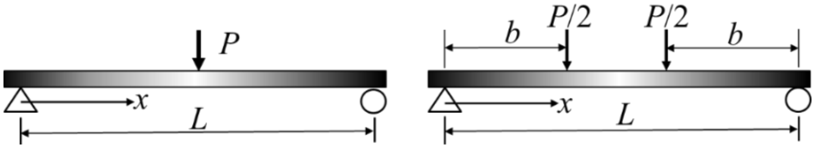

(a) (b)

Fig. 9. Typical load definitions: (a) three-, and (b) four-point bending.

The moment equilibrium of the concrete and FRP segments gives:

$$\frac{dM_C(x)}{dx} - v(x)\frac{h_C}{2} + r(x)\frac{dx}{2} + V_C(x) = 0 \tag{8a}$$

$$\frac{dM_F(x)}{dx} - v(x)\frac{h_F}{2} - r(x)\frac{dx}{2} + V_F(x) = 0 \tag{8b}$$

where $M_c(x)$ and $M_F(x)$ are the moments carried by the concrete and FRP, respectively; h_c and h_F are the depths of concrete and FRP, respectively (see Fig. 4a); $r(x)$ is the normal force along the FRP-concrete interface.

According to assumption (ii), the curvature compatibility of the concrete and FRP gives:

$$\phi(x) = \frac{M_F(x)}{E_{Fx}I_F} = \frac{M_C(x)}{E_C I_C} \tag{9}$$

where E_{Fx} is the elastic modulus of FRP in x direction; I_F and I_C are the moment inertias of FRP and concrete, respectively; E_C is the elastic modulus of concrete; $\phi(x)$ is the curvature of the beam.

For the constitutive relationships of the materials, linear elastic properties of the FRP and concrete are adopted. The FRP is inherently linear elastic; the stresses in the concrete remain low before the FRP fails with a shear failure, as supported by the test results in Section 2 and previous experiments in [8][11][21]. The longitudinal modulus of FRP is employed to compute the sectional rigidity, assuming the compressive and tensile moduli of FRP are the same. Strains in the concrete $\varepsilon_C(x,y)$ and FRP $\varepsilon_F(x,y)$ are calculated from the moment and axial force as:

$$\varepsilon_C(x,y) = \frac{M_C(x)\left(\frac{h_C}{2} - y\right)}{E_C I_C} - \frac{N_C(x)}{E_C A_C}, 0 \le y \le h_C \tag{10a}$$

$$\varepsilon_F(x,y) = -\frac{M_F(x)\left(\frac{h_F}{2}+y\right)}{E_{Fx}I_F} + \frac{N_F(x)}{E_{Fx}A_F}, -h_F \le y \le 0 \tag{10b}$$

where A_C and A_F are the cross sectional areas of the concrete and FRP, respectively; y is vertical coordinate. Eq. (11) gives the strains in the concrete and FRP at the interface.

$$\varepsilon_C(x,0) = \frac{M_C(x)h_C}{2E_C I_C} - \frac{N_C(x)}{E_C A_C} \tag{11a}$$

$$\varepsilon_F(x,0) = -\frac{M_F(x)h_F}{2E_{Fx} I_F} + \frac{N_F(x)}{E_{Fx} A_F} \tag{11b}$$

The strain difference caused by the slip at the interface, denoted as $\varepsilon_{slip}(x)$, is calculated as:

$$\varepsilon_{slip}(x) = \varepsilon_C(x,0) - \varepsilon_F(x,0) \tag{12}$$

The strain difference is equal to the first order derivation of the relative slip at the interface:

$$s'(x) = \varepsilon_{slip}(x) \tag{13}$$

Substituting Eqs. (8), (9), (11), and (12) into (13),

$$s'(x) = \phi(x)h_o - \frac{N_C(x)}{E_C A_C} - \frac{N_F(x)}{E_{Fx} A_F} \tag{14}$$

where h_0 is the distance between the neutral axis of concrete and FRP, given by $h_0 = \frac{h_C + h_F}{2}$.

Solving Eqs. (6) and (14) yields:

$$\phi'(x) = \frac{V(x) - h_o k s(x)}{E_{Fx} I_o} = \frac{V(x)}{E_{Fx} I_o}[1 - m(x)] \tag{15}$$

where $I_0 = I_C/\alpha_E + I_F$, $\alpha_E = E_{Fx}/E_C$, and $m(x) = h_0 k s(x)/V(x)$.

At the supports (x = 0, L), $m(x) = m_0$, where m_0 is a dimensionless factor depending on the shear connection. The physical meaning of m_0 will be discussed in Section 4. Table 5 shows the solutions of m_0.

Plugging Eq. (14) in Eq. (15), the governing equation of the relative slip is obtained:

$$s''(x) - \alpha^2 s(x) = -\alpha^2 \beta V(x) \tag{16}$$

where $\alpha = \sqrt{kA_1/(E_{Fx}I_0)}$, $\beta = h_0/kA_1$, $A_1 = I_0/A_0 + h_0^2$, and $A_0 = A_F A_C/(\alpha_E A_F + A_C)$.

To solve Eq. (16), the boundary conditions are considered: $s(L/2) = 0$, and $\frac{ds(0)}{dx} = \frac{ds(L)}{dx} = 0$. Table

5 shows the solutions of interfacial slip under the three-point and four-point bending tests.

Table 5. Loads and corresponding solutions

Loads	Solution of $s(x)$	m_0	$m_{0,full}$
Fig. 9a	$\frac{\beta P}{2}\left[1-\cosh(\alpha x)/\cosh\left(\frac{\alpha L}{2}\right)\right], 0 < x < L/2$	$\frac{h_0^2}{A_1}\left[1-\mathrm{sech}\left(\frac{\alpha L}{2}\right)\right]$	$\frac{h_0^2}{A_1}$
Fig. 9b	$\begin{cases} \frac{\beta P}{2}\{1-\mathrm{sech}\left(\frac{\alpha L}{2}\right)\cosh[\alpha\left(\frac{L}{2}-b\right)]\cosh(\alpha x)\}, 0 < x < b \\ \frac{\beta P}{2}\mathrm{sech}\left(\frac{\alpha L}{2}\right)\sinh[\alpha\left(\frac{L}{2}-x\right)]\sinh(\alpha b), b < x < L/2 \end{cases}$	$\frac{h_0^2}{A_1}\left[1-\mathrm{sech}\left(\frac{\alpha L}{2}\right)\cosh[\alpha\left(\frac{L}{2}-b\right)]\right]$	$\frac{h_0^2}{A_1}$

4.2. Shear stress distributions in FRP and concrete

Fig. 10 shows the normal stress distribution in the FRP-concrete composite section. According to equation of equilibrium of the infinitesimal (*dx*) in *x* direction, Eq. (17) is obtained:

$$\tau_F(x,y)t(y)dx + \int_{-h_F}^{y} \sigma_F(x,y)t(y)dy = \int_{-h_F}^{y} [\sigma_F(x,y) + \frac{\partial \sigma_F(x,y)}{\partial x}dx]\cdot t(y)dy \tag{17}$$

where $\tau_F(x,y)$ is the shear stress of FRP; $t(y)$ is the thickness of FRP web or FRP width; $\sigma_F(x,y)$ is the normal stress of FRP.

Simplifying Eq. (17) and cancelling out the same items yield:

$$\tau_F(x,y)t(y) = \int_{-h_F}^{y} \frac{\partial \sigma_F(x,y)}{\partial x} t(y)dy \tag{18}$$

According to the Hook's law, the stress in the FRP can be expressed as:

$$\sigma_F(x,y) = E_{Fx}\varepsilon_F(x,y) \tag{19}$$

Substituting Eqs. (10a) and (19) to Eq. (18) yields:

$$\tau_F(x,y) = [V(x) - h_0 ks(x)]\frac{S_F(y)}{I_0 t(y)} + \frac{ks(x)}{t(y)}\cdot\frac{A_F(y)}{A_F}, -h_F \le y \le 0 \tag{20}$$

where $S_F(y) = \int_{-h_F}^{y} -\left(y + \frac{h_F}{2}\right)t(y)dy$ and $A_F(y) = \int_{-h_F}^{y} t(y)dy$.

Analogously, the shear stress of concrete is written as:

$$\tau_C(x,y) = [V(x) - h_0 ks(x)]\frac{S_C(y)}{\alpha_E I_0 b_C} + \frac{ks(x)}{b_C}\cdot\frac{h_C - y}{h_C}, -h_F \le y \le 0 \tag{21}$$

where $\tau_C(x,y)$ is the shear stress of concrete, and $S_C(y) = \int_{y}^{h_C} b_C\left(y - \frac{h_C}{2}\right)dy$.

Eq. (20) can be used to obtain the shear stress of FRP web ($-h_F + t_{Flange} \leq y \leq -t_{Flange}$), where t_{Flange} is the thickness of FRP flange:

$$\tau_{F,web}(x,y) = \frac{V(x)}{t_{web}}\left[[1 - m(x)]\frac{S_F(y)}{I_0} + m(x)\frac{A_F(y)}{h_0 A_F}\right] \tag{22}$$

The maximum shear stress occurred symmetrically at two supports ($x = 0, L$), thus,

$$\tau_{F,web}(0,y) = \frac{P}{2t_{web}}\left[(1 - m_0)\frac{S_F(y)}{I_0} + m_0\frac{A_F(y)}{h_0 A_F}\right] \tag{23}$$

To locate the maximum shear stress, it is enforced that:

$$\frac{\partial \tau_{F,web}(0,y)}{\partial y} = 0 \tag{24}$$

Solving Eq. (24) gives the maximum shear stress (τ_{max}) at the point $(0, y_0)$, where y_0 is given by:

$$y_0 = \frac{I_0}{A_F h_0} \cdot \frac{1}{\frac{1}{m_0} - 1} - \frac{h_F}{2} \tag{25}$$

The analytical and experimental results of y_0 for the specimens in Section 2 are listed in Table 4. It can be deduced from the computation of y_0 that $-h_F/2 \leq y \leq -t_{Flange}$, meaning that the maximum shear stress (τ_{max}) is within the FRP web (Fig. 11a); $y \geq -t_{Flange}$, meaning that the maximum shear stress is within the FRP web-flange joint (Fig. 11b). Different failure criteria were used to predict the failure of FRP in past research. In this study, since the normal stress in the FRP web is far less than its strength, the maximum shear stress failure criterion is employed.

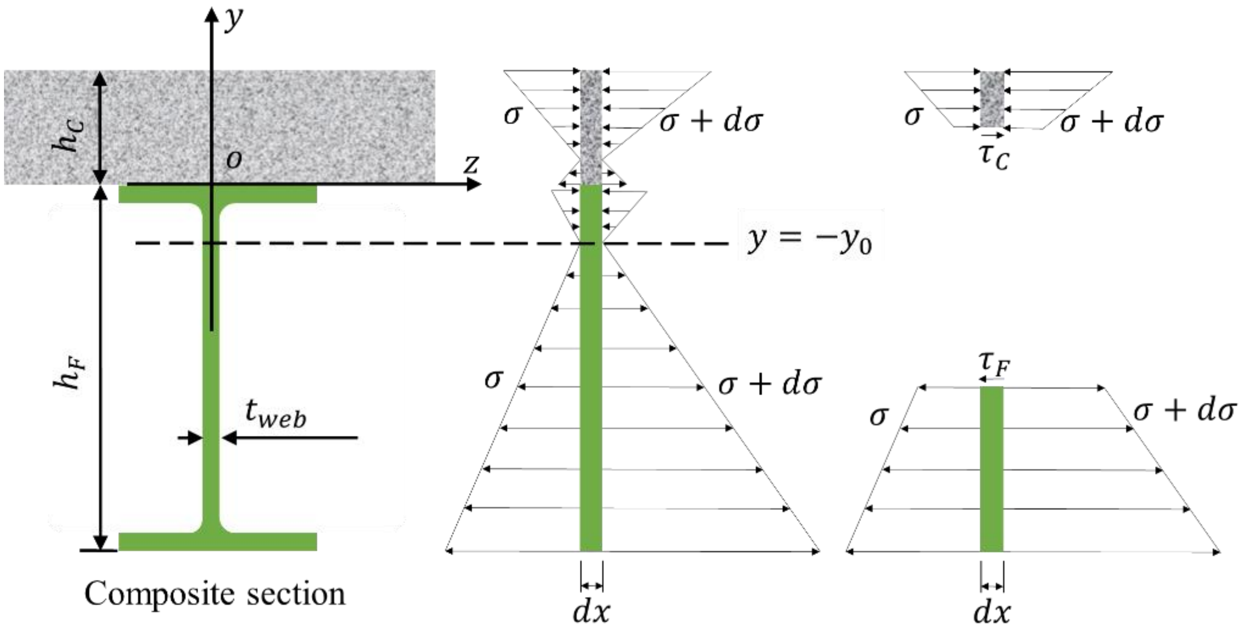

Fig. 10. The distribution of the normal stress in the FRP-concrete composite section.

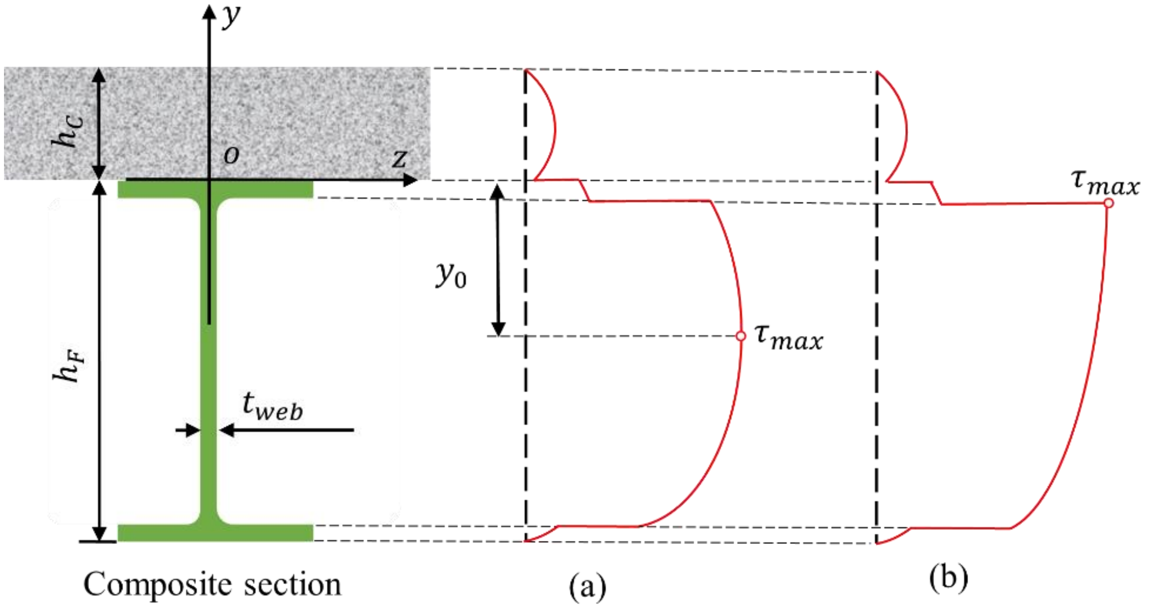

Fig. 11. The maximum shear stress may occur in (a) the FRP web, and (b) the FRP web-flange joint.

4.3. Validation

Table 6 compares the shear strengths of specimens determined using the derived formulae and experiments [5][12]. The average result of $\frac{\tau_{max}}{S_{xy}}$ is 1.023 with a coefficient of variation (CoV) of 0.162. The analytical results of y_0 are in Table 4, which shows good agreement with the measured values. The relatively high variation of $\frac{\tau_{max}}{S_{xy}}$ of the specimens in [5] is likely due to incorrect material strength data. For the rest of the specimens, $\frac{\tau_{max}}{S_{xy}}$ is close to 1.0, and CoV is small, revealing that Eq. (22) can be used to compute the shear stress. τ_{max} of specimen HB-T is 22% lower than S_{xy}, which is because the thick and wide concrete slab had some cracks when FRP failed. The influence of these cracks indicates that concrete damage should be considered when the concrete is thick compared with the depth of the FRP, which will be further researched.

Fig. 12 compares the shear strength of the FRP with the shear stress distribution along the depth of the FRP profile of each specimen listed in Table 6. In each specimen, the shear stress distribution is nonuniform and shows a parabolic shape. The shear stresses in the concrete are significantly lower than the shear stresses in the FRP profiles. This is associated with the larger thickness of the concrete.

Table 6. Validation of shear stress in tested specimens with shear failure

Ref.	Specimen	$b_C \times h_C$ (mm×mm)	h_F (mm)	b_F (mm)	t_{Flange} (mm)	t_{web} (mm)	p (mm)	Push-out specimen	K (kN/mm)	L (m)	m_0	V_{test} (kN)	S_{xy} (MPa)	τ_{max} (MPa)	$\frac{\tau_{max}}{S_{xy}}$	η_F	η_{SD}
This study	HB-1	100×100	200	100	10	10	140	P-HSB [8]	9.63	2.6	0.597	18.7	9.2	9.43	1.025	0.85	1.15
	HB-2	100×100	200	100	10	10	170		9.63	2.6	0.582	19.5	9.2	9.93	1.079	0.86	1.10
	HB-3	100×100	200	100	10	10	220		9.63	2.6	0.558	17.9	9.2	9.20	1.000	0.87	1.18
[8]	HB	730×60	150	100	10	7	120	P-SB-SIP [8]	*a	2.1	0.538	49.6	25.3	28.30	1.119	0.59	1.29
	HB-T	730×110	150	100	10	7	120		*a	2.1	0.302	74.8	25.3	19.66	0.777	0.25	2.03
	HB-R	730×60	150	100	10	7	120		*a	2.1	0.538	47.3	25.3	27.19	1.075	0.59	1.35
[5]	HB1	400×100	120	60	10	10	130	SCS2 [5]	20	4.0	0.585	91.0	47.1	39.98	0.849	0.55	1.87
	HB3	400×100	120	60	10	10	130	SCS3 [5]	12	1.8	0.316	148.1	47.1	67.87	1.441	0.48	1.47
	HB5	400×100	120	60	10	10	130	SCS6 [5]	*b	1.8	0.592	87.9	47.1	38.62	0.820	0.55	2.01
[12]	M1-HB3	400×50	120	6	8	8	300	M6 [12]	5.78*c	1.8	0.329	81.1	35.0	33.62	0.961	0.63	1.31
	M1-HB4	400×50	120	6	8	8	300		5.78*c	1.8	0.329	85.6	35.0	35.48	1.014	0.63	1.24
	M2-HB3	400×50	120	6	8	8	300		5.78*c	1.8	0.336	89.8	35.0	37.21	1.063	0.63	1.19
	M2-HB4	400×50	120	6	8	8	300		5.78*c	1.8	0.329	91.3	35.0	37.84	1.081	0.63	1.16
	Average														1.023	0.63	1.41
	CoV														0.162	0.27	0.24

*a. Full composite action was employed in the specimens because SIP formwork was used and there was no slip at the interface in [8].

*b. Full composite action was ensured by using epoxy resin as connection SCS6 in [5].

*c. The value of K was assumed as 80% of M10 stud, because of lack of push-out test data for the studs.

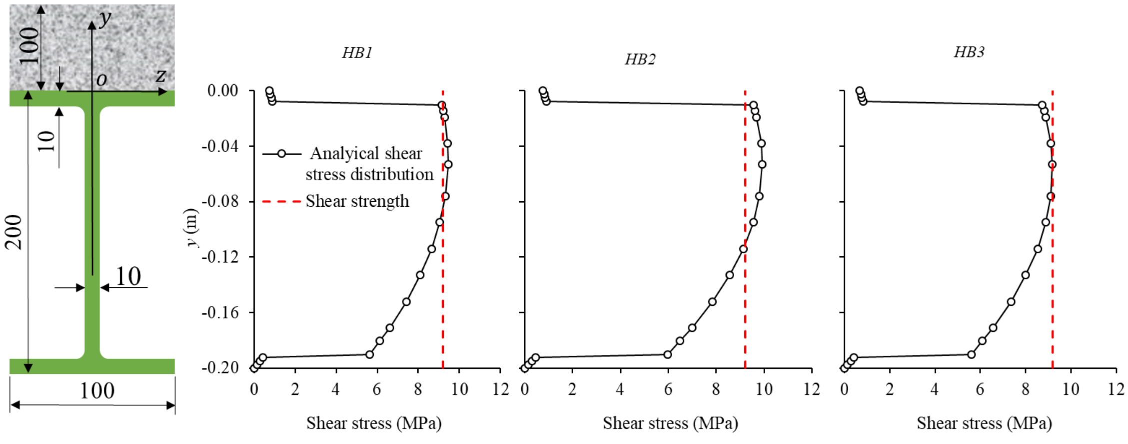
100
y
o
z
10
200
10
100
HB1
HB2
HB3
0.00
-0.04
-0.08
-0.12
-0.16
-0.20
y (m)
Analyical shear stress distribution
Shear strength
0 2 4 6 8 10 12
Shear stress (MPa)

(a)

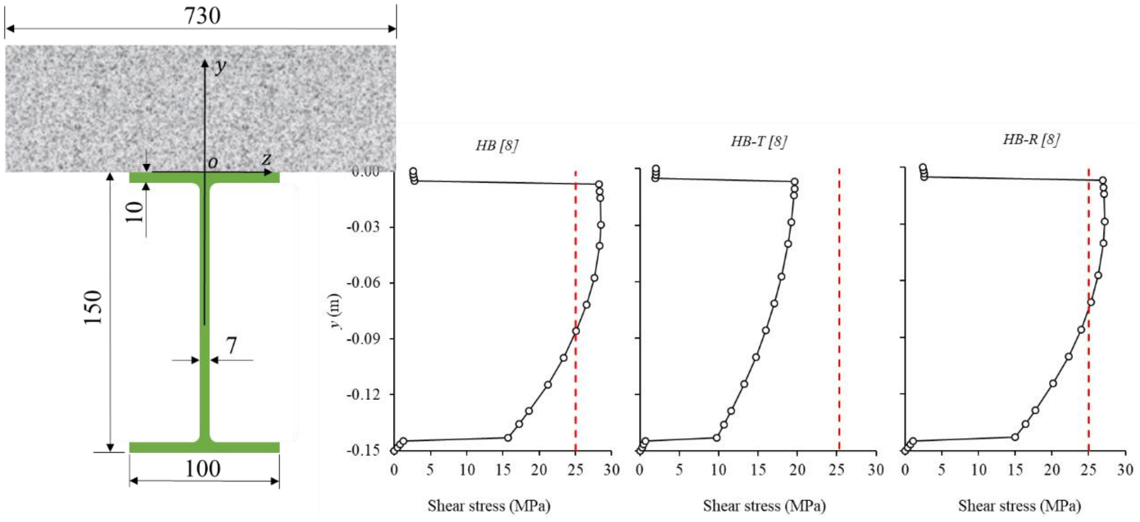
730
y
o
z
10
150
7
100
HB [8]
HB-T [8]
HB-R [8]
0.00
-0.03
-0.06
-0.09
-0.12
-0.15
y (m)
0 5 10 15 20 25 30
Shear stress (MPa)

(b)

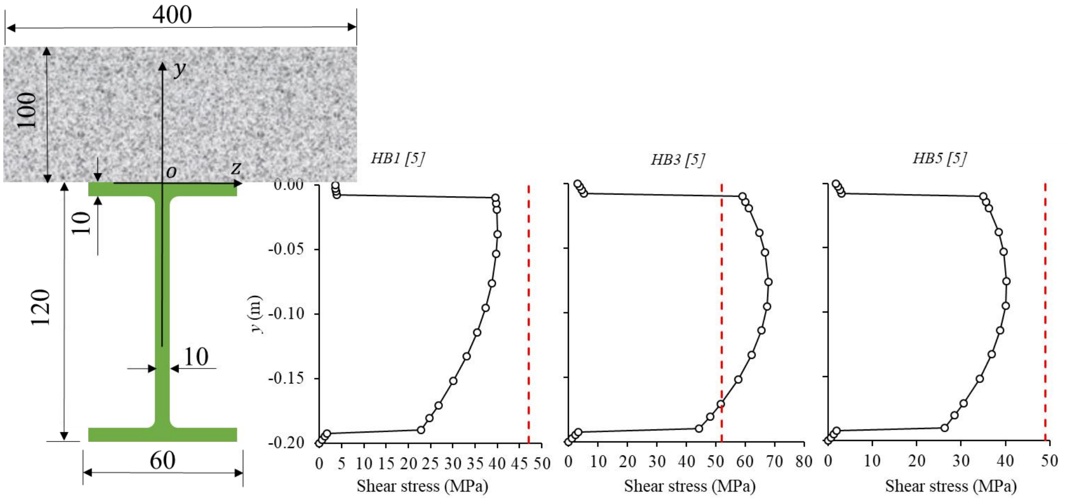
400
100
y
o
z
10
120
10
60
HB1 [5]
HB3 [5]
HB5 [5]
0.00
-0.05
-0.10
-0.15
-0.20
y (m)
0 5 10 15 20 25 30 35 40 45 50
0 10 20 30 40 50 60 70 80
0 10 20 30 40 50
Shear stress (MPa)

(c)

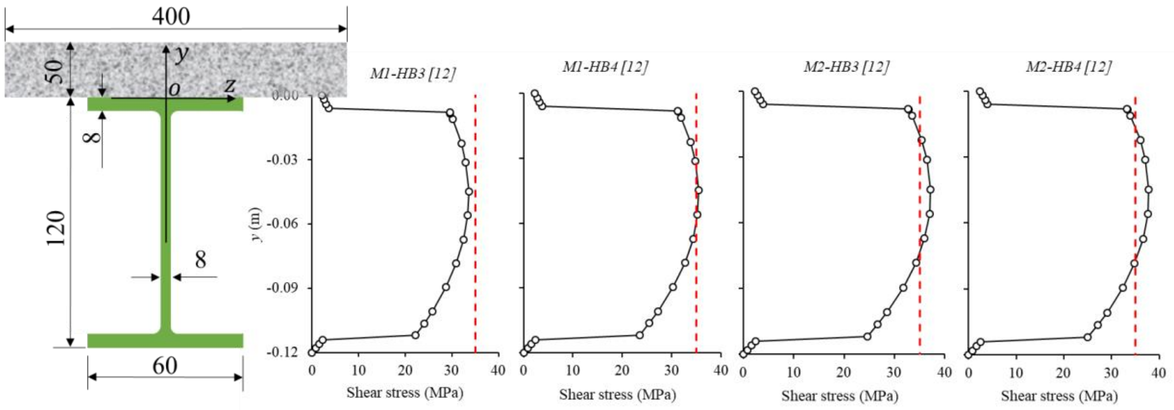

(d)

Fig. 12. Analytical shear stress distribution of FRP at failure load of specimens in: (a) the present study, (b) [8], (c) [5], and (d) [12]

5. Discussions

Based on the formulae derived in Section 3, parametric studies are performed to understand the effects of key parameters on the shear behavior and discuss the composite actions. The investigated parameters include the space of adjacent connectors, the thickness of FRP web, longitudinal modulus of FRP, and thickness of the concrete slab.

5.1. Parametric study

The geometry and materials in specimens HB1 to HB3 are used as the control in the parametric study for a FRP-concrete composite deck: h_C = 100 mm, h_F = 200 mm, $b_C = b_F$ = 100 mm, $t_{Flange} = t_{web}$ = 10 mm, p = 200 mm, K = 8 kN/mm, L = 2.6 m, E_{Fx} = 12.8 GPa, and E_c = 29.5 GPa.

Fig. 13 shows that as the space of adjacent connectors, p, increases from 0 to 5 m, m_0 decreases from 0.65 to 0.10. At p = 0, the FRP-concrete composite deck has full composite action, resulting in $m_0 = \frac{h_0^2}{A_1}$. As p approaches to infinite, there is no composite action, and m_0 decreases to 0. Thus, it is rational to use the ratio of m_0 and $\frac{h_0^2}{A_1}$ to characterize the degree of composite action of the composite sections: full composite action is represented by $\frac{m_0}{(h_0^2/A_1)}$ = 1.0; non-composite action is represented by $\frac{m_0}{(h_0^2/A_1)}$ = 0.

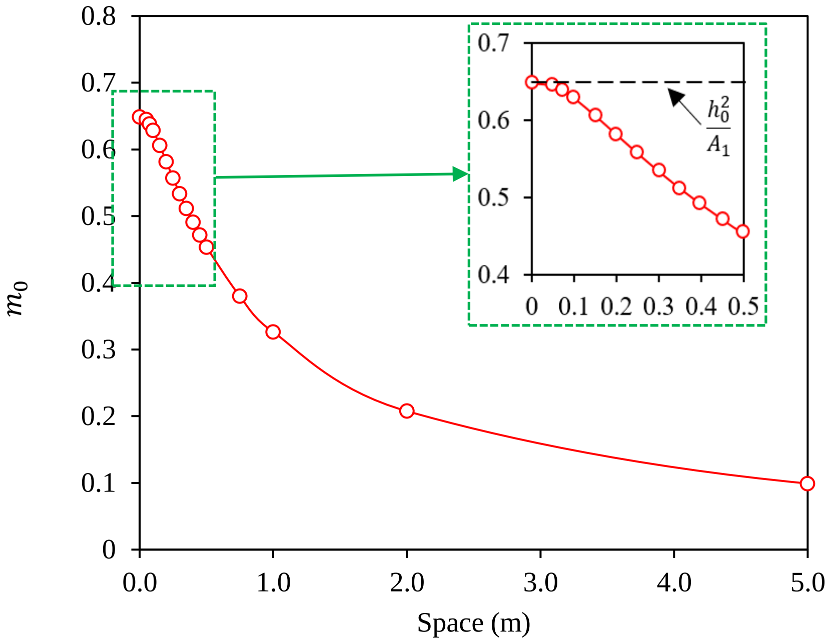

Fig. 13. The relationship between the space of connector and m_0.

Fig. 14 shows that as m_0 increases from 0 to h_0^2/A_1(=0.65), the maximum shear stress decreases, and the neutral axis of the FRP moves from the center of the FRP web to the upper flange-web joint. For a beam with the same geometry and material properties, as the shear connection changes from non-composite action to full-composite action ($\frac{m_0}{(h_0^2/A_1)}$ increases from 0 to 1), the maximum shear stress decreases from 12.9 MPa to 9.4 MPa. Therefore, the shear connection plays a significant role in the shear capacity of the FRP-concrete composite sections.

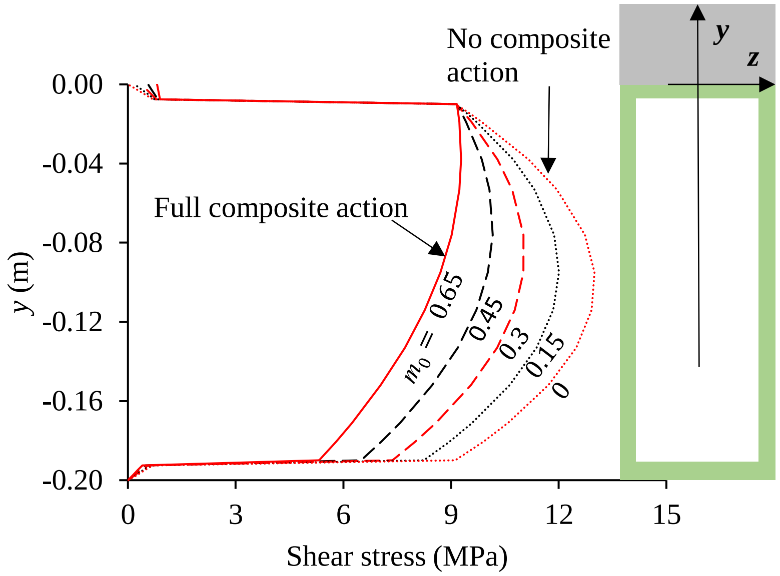

Fig. 14. Effect of composite action degree on the shear stresses in FRP-concrete composite section.

Fig. 15 shows the effects of the thickness of FRP web, longitudinal modulus of FRP, and thickness of the concrete slab on the maximum shear stress. As the thickness of FRP web (t_{web}) increases from 4 mm to 30 mm, the maximum shear stress decreases from 17.4 MPa to 3.1 MPa (see Fig. 15a). As the longitudinal modulus of FRP (E_{Fx}) increases from 2.5 GPa to 100 GPa, τ_{max} increases from 4.1 MPa to 9.8 MPa (see Fig. 15b). As the thickness of the concrete slab (h_C) increases from 0.01 m to 0.13 m, the maximum shear stress decreases from 13.9 MPa to 4.6 MPa (see Fig. 15c).

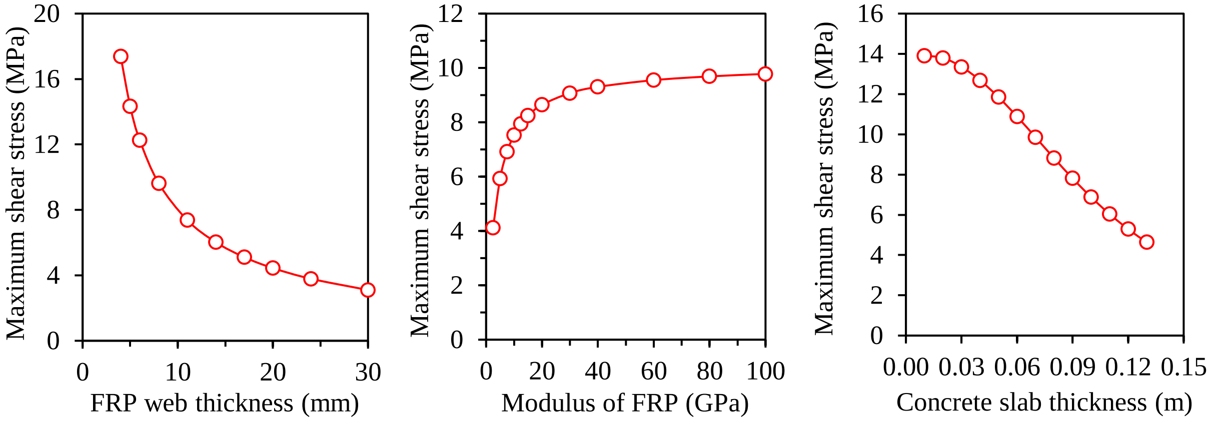

(a) (b) (c)

Fig. 15. Parametric study of the effect of (a) thickness of FRP web, (b) longitudinal modulus of FRP, and (c) height of concrete slab on the maximum shear stress.

5.2. Composite action

Fig. 16 plots the relationship between αL and $\frac{m_0}{(h_0^2/A_1)}$ under three-point bending. With $\alpha = 0$, it can be calculated that $m_0 = 0$ and $y_0 = -h_F/2$, which means the neural axis locates in the center of the FRP section. Previous tests showed that strong shear connections along the FRP-concrete interface were obtained using adhesive-studs mixed connection [5], FRP shear keys [32], or perforated FRP ribs [24]. With a high degree of composite action, $\alpha L \geq 4$, and $\frac{m_0}{(h_0^2/A_1)} \geq 0.963$. Since 0.963 is close to 1.0, the above equations can be reconstructed by replacing m_0 with $m_{0,full}$ (see Table 5) when $\alpha L \geq 4$.

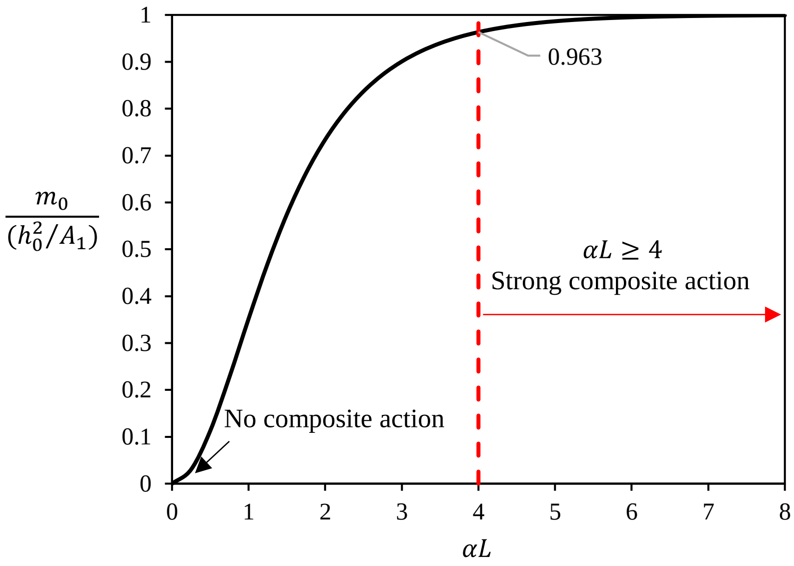

Fig. 16. The influence of the degree of composite action.

6. Design Method

At the supports, the shear forces carried by concrete and FRP are obtained by integrating the shear stress in the height (y) direction:

$$V_C = \int_0^{h_C} \tau_C\,(0, y_0) b_C dy = \frac{P}{2}\left[(1 - m_0)\frac{I_C/\alpha_E}{I_0} + m_0\frac{h_C}{h_C + h_F}\right] \qquad (26a)$$

$$V_F = \int_{-h_F}^{0} \tau_F\,(0, y_0) t(y) dy = \frac{P}{2}\left[(1 - m_0)\frac{I_F}{I_0} + m_0\frac{h_F}{h_C + h_F}\right] \qquad (26b)$$

where b_C is the width of concrete. It should be noted that the shear lag effect has been observed and analyzed in steel-concrete composite sections where wider concrete slabs were used and higher stress level were reached, so an effective width was used instead of the whole width of concrete [33][34][35]. But in this study, effective width was not considered. Further studies about the shear lag effect of concrete slab and FRP flange can be conducted, and the effective width can be used to replace b_C here.

Rewriting Eq. (26) gives the contributions of concrete and FRP girder:

$$V_C = \frac{P}{2}\eta_C \tag{27a}$$

$$V_F = \frac{P}{2}\eta_F \tag{27b}$$

where, η_C and η_F denote the contribution ratios of concrete and FRP, respectively ($\eta_C + \eta_F$=1):

$$\eta_C = (1 - m_0)\frac{I_C/\alpha_E}{I_0} + m_0\frac{h_C}{h_C + h_F} \tag{28a}$$

$$\eta_F = (1 - m_0)\frac{I_F}{I_0} + m_0\frac{h_F}{h_C + h_F} \tag{28b}$$

Eqs. (27) and (28) indicate that the contributions of FRP and concrete depend on the degree of composite action (related to m_0) and the flexural rigidity ratio ($\frac{I_C/\alpha_E}{I_0}$ or $\frac{I_F}{I_0}$), assuming that the elastic modulus and height ratio ($\frac{h_C}{h_C+h_F}$ or $\frac{h_F}{h_C+h_F}$) are constant. It should be noted that when thicker and wider concrete slab was used, the concrete will crack under tensile stress, which may reduce the moment inertias of concrete, see I_C in Eqs. (9) and (23a). So more test data for wider and thicker concrete slab are needed to modify the shear capacity of concrete slab.

In I_F, the contribution of the FRP web can be neglected. Therefore, Eq. (27b) can be rewritten as:

$$\eta_F = (1 - m_0)\frac{1}{1 + \frac{b_c h_c^3}{24\alpha_E t_F b_F h_F^2}} + m_0\frac{h_c}{H} = \frac{1 - m_0}{1 + \frac{1}{12\alpha_E \alpha_1 \alpha_2^2}} + \frac{m_0}{1 + \alpha_2} \tag{29}$$

where $\alpha_1 = \frac{2t_F b_F}{b_c h_c}$, which is the ratio of cross sectional area of FRP flanges over concrete; $\alpha_2 = \frac{h_F}{h_c}$, which is the ratio of height of FRP girder over concrete; η_F can be used to evaluate the composite action between FRP and concrete.

Eq. (29) shows that m_0 and α_2 are the two main parameters that determine the contribution of FRP on the shear capacity. The value of η_F using Eq. (27b) has an average value of 0.63, as shown in Table 5. In this study, η_F is larger than 0.85, because the width of concrete is small; the average result of η_F is less than 0.63 for the rest of specimens in [5][12], because the section of concrete is wide compared with the FRP.

The design equation can be given by modifying Eq. (1):

$$V = \frac{1}{\eta} A_{web} S_{xy} \tag{30}$$

Herein, rewriting Eq. (30) gives:

$$\eta = \frac{A_{web} S_{xy}}{V} \tag{31}$$

Considering the ultimate state $S_{xy} = \tau_{max}$, η is expressed as:

$$\eta = \frac{A_{web} \tau_{max}}{V} \tag{32}$$

Rewriting Eq. (32) gives:

$$\eta = \eta_F \frac{A_{web} \tau_{max}}{V_F} = \eta_F \frac{\tau_{max}}{\tau_{avg}} = \eta_F \eta_{SD} \tag{33}$$

where $\tau_{avg} = V_F / A_{web}$, which is the average shear stress of FRP web, and $\eta_{SD} = \tau_{max}/\tau_{avg}$ is the ratio of the maximum shear stress over the average shear stress.

It is interesting that Eq. (1) can be obtained from Eqs. (30) and (33) by enforcing: η_F =1.0 and η_{SD}=1.0. Similarly, Eq. (2) can be obtained by enforcing: η_F =1.0 and η_{SD}=1.5. Eqs. (30) and (33) show that there are two factors that affect the accuracy, which are the contribution of the concrete and the nonuniform distribution of shear stress along the FRP profile. η_F can be quantified using Eq. (27b) or approximately by Eq. (29). The value of η_{SD} mainly depends on the location of the neutral axis and the distribution of shear stress. In order to get a design value for η_{SD}, the beams in Table 5 are used to inversely calibrate η_{SD}. To be specific, the following equation can be used:

$$\eta_{SD} = \frac{\eta}{\eta_F} = \frac{A_{web} S_{xy}}{\eta_F V_{u.test}} \tag{34}$$

It can be seen that η_{SD} has an average value of 1.41, which is between 1.0 and 1.5 given by Eqs. (1) and (2), respectively. Herein, it is suggested that $\eta_{SD} = 1.41$ can be used for the design. Therefore, the final design equation is given as:

$$V = \frac{1}{1.41\eta_F} A_{web} S_{xy} \tag{35}$$

However, since it remains unclear whether the value of 1.41 is suitable for all cases. Further research is needed to obtain more test data to determine η_{SD}. The design procedure can be depicted using Fig. 17.

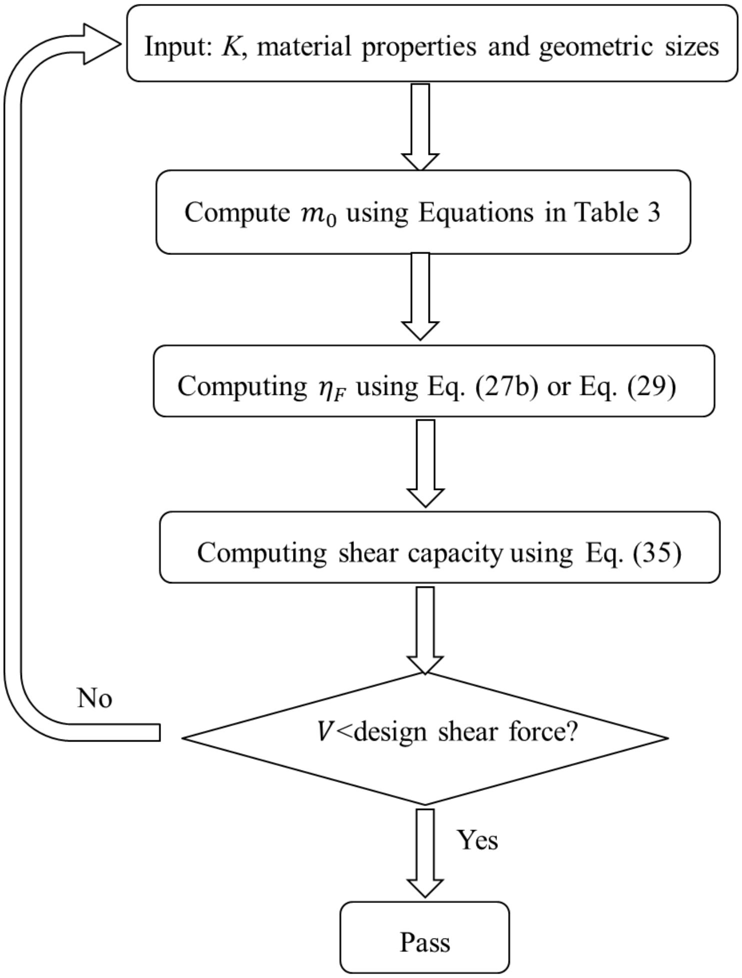

Fig. 17. The procedure to design an FRP-concrete composite section with adequate shear capacity.

7. Conclusions

This study investigates the shear behaviors of FRP-concrete composite sections by experiments and analysis. Practical formulae were developed to predict the shear capacity of the composite sections. Based on the above experimental and analytical investigations, the following conclusions are drawn:

(i) The shear failure mode of FRP-concrete composite sections is brittle and characterized by the fracture along the horizontal direction at FRP webs or the upper web-flange joint.

(ii) When steel studs are used to connect the FRP and concrete, partial composite action is achieved, which yields to an increase of shear stress compared with full composite action scenario.

(iii) The partial interaction between FRP and concrete is modeled by considering slip effect and composite action degree that depends on the stiffness and spacing of the shear connectors. A closed-form equation for shear capacity of the composite sections is derived based on the maximum shear strength failure criterion of FRP webs.

(iv) The derived analytical equations can provide adequate predictions of the shear capacity and shear stress distributions in the FRP-concrete composite sections. Based on the parametric analysis, a simplified equation was derived for design.

(v) Parametric study shows that the shear capacity of the FRP-concrete composite sections is significantly affected by the characteristics of the shear connectors (size, slip stiffness, and spacing), the thickness of FRP web(s), and the thickness of concrete slab.

In the future, more tests are suggested to advance the understanding of the cracking of concrete slab when wider and thicker concrete slab was used. Thus possible modification can be made on the parameter η_F in the proposed design equation. Also, effective width can be used for concrete slab and FRP flange when the shear lag effect is observed for larger or full-scale FRP-concrete hybrid sections.

8. Acknowledgments

The authors would like to thank the authors of reference [5] for providing the shear strength data of their specimens. Thanks also go to Mr. Zhitao Chen and Mr. Songlin Li, formerly students advised by the corresponding author, for their contribution to the tests.

9. Declaration of interests

Declarations of interest: none.

10. Funding

This work was supported by the National Natural Science Foundation of China (Grant No. 51678140).

11. CRediT author statement

Xingxing Zou: Conceptualization, Methodology, Experimental test, Writing- Original draft preparation. **Peng Feng**: Supervision, Methodology, Funding acquisition. **Yi Bao**: Methodology, Writing- Reviewing and Editing. **Jingquan Wang**: Supervision, Funding acquisition, Laboratory work support, **Haohui Xin**: Writing- Reviewing.

12. Data availability

The raw data required to reproduce these findings cannot be shared at this time as the data is a part of the ongoing funded project.

13. References

[1] Hollaway, L. C. (2010). A review of the present and future utilisation of FRP composites in the civil infrastructure with reference to their important in-service properties. Construction and building materials, 24(12), 2419-2445.

[2] Kong, S. Y., Yang, X., and Lee, Z. Y. (2018). Mechanical performance and numerical simulation of GFRP-concrete composite panel with circular hollow connectors and epoxy adhesion. Construction and Building Materials, 184, 643-654.

[3] Nguyen, H., Mutsuyoshi, H., and Zatar, W. (2015). Hybrid FRP-UHPFRC composite girders: Part 1–Experimental and numerical approach. Composite Structures, 125, 631-652.

[4] Gutiérrez, E., Primi, S., Mieres, J. M., and Calvo, I. (2008). Structural testing of a vehicular carbon fiber bridge: Quasi-static and short-term behavior. Journal of Bridge Engineering, 13(3), 271-281.

[5] Correia, J. R., Branco, F. A., and Ferreira, J. (2009). GFRP-concrete hybrid cross-sections for floors of buildings. Engineering Structures, 31(6), 1331-1343.

[6] Keller, T. (2001). Recent all-composite and hybrid fibre-reinforced polymer bridges and buildings. Progress in Structural Engineering and Materials, 3(2), 132-140.

[7] Seible, F., Karbhari, V. M., and Burgueño, R. (1999). Kings stormwater channel and I-5/Gilman bridges, USA. Structural Engineering International, 9(4), 250-253.

[8] Zou, X., Feng, P., Wang, J., Wu, Y., and Feng, Y. (2018). FRP stay-in-place form and shear key connection for FRP-concrete hybrid beams/decks. Composite Structures, 192, 489-499.

[9] Ulloa, F. V., Medlock, R. D., Ziehl, P. H., and Fowler, T. J. (2004). Hybrid bridges in Texas. Concrete international, 26(5), 38-43.

[10] Keller, T., Schaumann, E., and Vallée, T. (2007). Flexural behavior of a hybrid FRP and lightweight concrete sandwich bridge deck. Composites Part A: Applied Science and Manufacturing, 38(3), 879-889.

[11] Siwowski, T., Kaleta, D., and Rajchel, M. (2018). Structural behaviour of an all-composite road bridge. Composite Structures, 192, 555-567.

[12] Neagoe, C. A., Gil, L., and Pérez, M. A. (2015). Experimental study of GFRP-concrete hybrid beams with low degree of shear connection. Construction and Building Materials, 101, 141-151.

[13] Zhang, S., Xue, W. C., & Liao, X. (2019). Theoretical analysis on long-term deflection of GFRP-concrete hybrid structures with partial interaction. Composite Structures, 216, 1-11.

[14] Sánchez-Aparicio, L. J., Ramos, L. F., Sena-Cruz, J., Barros, J. O., & Riveiro, B. (2015). Experimental and numerical approaches for structural assessment in new footbridge designs (SFRSCC–GFPR hybrid structure). Composite Structures, 134, 95-105.

[15] Chakrabortty, A., Khennane, A., Kayali, O., & Morozov, E. (2011). Performance of outside filament-wound hybrid FRP-concrete beams. Composites Part B: Engineering, 42(4), 907-915.

[16] Fiberline. 2002. Design manual, Kolding, Denmark.

[17] Strongwell. 2007. Design manual, Strongwell Corporation, Bristol, Va.

[18] Top Glass. 2008. “Technical data.” http://www.topglass.it/.

[19] Creative Pultrusions. 2008. “Technical data.” http://www.creativepultrusions.com/

[20] Meier, U., Triantafillou, T. C., and Deskovic, N. (1995). Innovative design of FRP combined with concrete: short-term behaviour. Journal of Structural Engineering, 121(7), 1069-78.

[21] El-Hacha, R., and Chen, D. (2012). Behaviour of hybrid FRP-UHPC beams subjected to static flexural loading. Composites Part B: Engineering, 43(2), 582-593.

[22] Iskander, M., El-Hacha, R., and Shrive, N. (2018). Governing failure criterion of short-span hybrid FRP-UHPC beams subjected to high shear forces. Composite Structures, 185, 123-131.

[23] Zou, X., Feng, P., and Wang, J. (2018). Bolted shear connection of FRP-concrete hybrid beams. Journal of Composites for Construction, 22(3), 04018012.

[24] Zou, X., Feng, P., and Wang, J. (2016). Perforated FRP ribs for shear connecting of FRP-concrete hybrid beams/decks. Composite Structures, 152, 267-276.

[25] Nanjing Kangte Composite Material. http://www.ktc-fiberglass.com/ (accessed in Dec. 2019)

[26] GB 50608–2010. Technical Code for Infrastructure Application of FRP Composites. China Architecture & Building Press: Beijing, China, 2011. (in Chinese).

[27] GB 50010-2010. Code for Design of Concrete Structures. China Building Industry Press, Beijing, China, 2011 (in Chinese).

[28] Nie, J., and Cai, C. S. (2003). Steel–concrete composite beams considering shear slip effects. Journal of Structural Engineering, 129(4), 495-506.

[29] Schnabl, S., Saje, M., Turk, G., and Planinc, I. (2007). Analytical solution of two-layer beam taking into account interlayer slip and shear deformation. Journal of Structural Engineering, 133(6), 886-894.

[30] Johnson, R. P., Molenstra, N., & EPPIB. (1991). Partial shear connection in composite beams for buildings. Proceedings of the Institution of Civil Engineers, 91(4), 679-704.

[31] Wang, S., Tong, G., and Zhang, L. (2017). Reduced stiffness of composite beams considering slip and shear deformation of steel. Journal of Constructional Steel Research, 131, 19-29.

[32] Alachek, I., Reboul, N., and Jurkiewiez, B. (2019). Experimental and finite element analysis of the long-term behaviour of GFRP-concrete hybrid beams fabricated using adhesive bonding. Composite Structures, 207, 148-165.

[33] Chen, Y., Dong, J., Xu, T., Xiao, Y., Jiang, R., and Nie, X. (2019). The shear-lag effect of composite box girder bridges with corrugated steel webs and trusses. Engineering Structures, 181, 617-628.

[34] Amadio, C., Fedrigo, C., Fragiacomo, M., and Macorini, L. (2004). Experimental evaluation of effective width in steel–concrete composite beams. Journal of Constructional Steel Research, 60(2), 199-220.

[35] Zhu, L., and Su, R. K. L. (2017). Analytical solutions for composite beams with slip, shear-lag and time-dependent effects. Engineering Structures, 152, 559-578.